APPLICATION OF MAGNETIC RESONANCE RADIOMICS PLATFORM (MRP) FOR MACHINE LEARNING BASED FEATURES EXTRACTION FROM BRAIN TUMOR IMAGES

IDOWU, B. A., DADA, O. M., &AWOJOYOGBE, O. B.
Department of Physics,
Federal University of Technology, PMB 65, Minna, Nigeria.
E-mail: dadamichael@futminna.edu.ng

Abstract

This study investigated the implementation of magnetic resonance radiomics platform (MRP) for machine learning based features extraction from brain tumor images. Magnetic resonance imaging data publicly available in The Cancer Imaging Archive (TCIA) were downloaded and used to perform image Coregistration, Multi-Modality, Images interpolation, Morphology and Extraction of radiomic features with MRP tools. Radiomics analyses were then applied to the data (containing AX-T1-POST, Diffusion weighted, AX-T2-FSE and AX-T2-FLAIR sequences) using wavelet decomposition principles. The results employing different configurations of low-pass and high-pass filters were exported to Microsoft excel data sheets. The exported data were visualized using MATLAB's classification learner tool. These exported data and the visualizations provide a new way of deep assessment of image data as well as easier interpretation of image scans. Findings from this study revealed that Machine learning Radiomics Platform is important in characterizing, visualizing and gives adequate information of a brain tumor.

Keywords: Brain tumor, Magnetic resonance imaging, Machine learning, Radiomics features extraction.

Introduction

A brain tumor is an abnormal growth of tissue in the brain or central spine that can disrupt proper brain function. Tumors can directly destroy healthy brain cells by invading them. Brain tumors are either malignant or benign (Merrel, 2012). A malignant tumor, also called brain cancer, usually grows rapidly and often invades or crowd's healthy areas of the brain. Benign brain tumors do not contain cancer cells and are usually slow growing. Malignant brain tumors can be classified into primary or secondary (metastatic) brain tumors. Primary brain tumors begin within the brain. A metastatic tumor is formed when cancer cells located elsewhere in the body break away and travel to the brain (http://www.cancer.gov/cancertopic). Medical imaging is the techniques and processes used to create images on the human body for various clinical purposes such as medical procedures and diagnosis or medical science including the study of normal anatomy and function (Ganguly*et al.,* 2010).

Machine learning is a rapidly evolving research field attracting increasing attention in the medical imaging community. Machine learning in radiology aims at training computers to recognize patterns in medical images and to support diagnosis by linking these patterns to clinical parameters such as treatment or outcome (Giger, 2018). These methods enable the quantification of disease extent and the prediction of disease colours with higher precision than is possible with the human eye. A machine-learning algorithm provides a reliable model for tumor classification and outcome prediction.

Magnetic Resonance Imaging uses a powerful magnetic field, radio frequency pulses and a computer to produce detailed pictures of organs, soft tissues, bone and virtually all other internal body structures. MRI provides detailed images that can detect brain abnormalities such as tumors and infection (Kanade&Gumaste, 2015). MRI has high sensitivity for detecting tumors and evaluating the surrounding area to some certain extent.

Magnetic Resonance Radiomic Platform (MRP-V4) is a software with a graphic user interface built on MATLAB programming environment for imaging, post-processing and for the calculation of adjustment of image resolution, Image intensity, and wavelength decomposition of MR radiomics features extraction in analyzing and visualizing of medical imaging (Lu*et al.*, 2018). MRP -V4 has the following the features:

i.   Data preparation and DICOM import
ii. Image Coregistration and Resolution adjustment
iii. Multi-Modality operation of Region of Interest (ROI) and Thresholding
iv. Extraction of Radiomics features (including wavelength decomposition)

Radiomics is a field in medicine that extracts large number of features from radiographic medical images using data characterization algorithms (Lambin*et al.,* 2012). These features extracted, have the potential to uncover disease characteristics that fail to be appreciated by the naked eye (Yip*et al.,* 2017). Radiomics features extraction of image, gives an insight to easily diagnosis and treatments of brain tumors without any difficulty. It helps radiologist with the diagnosis of both common and rare tumors and provide an additional independent information on visualization of tumors or heterogeneity which may have been difficult to access.

Medical imaging has the ability to extract useful information in human body which cannot be seen by human eye. In recent years' software like 3D Slicer, Statistical Parametric Mapping (SPM),Insight Segmentation and Registration Toolkit (ITK), Visualization Toolkit (VTK), have been developed. This work is limited to MRP-V4, it is used for the concept of underlying the process for both functional and morphological clinical images, that contain qualitative and quantitative information, that may reflect the underlying patho-physiology of a tissue. Radiomics analysis can be performed in brain tumour regions, metastatic lesions, as well as in normal tissues.

Aim and Objectives
This study is aim to extract numerical data from brain tumor images or medical images with the application of MR Radiomics platform (MRP-V4). The objectives of the work are to
(i)   Read and sort for DICOM of MRI, CT, and PET images, optimized for brain, breast, and chest imaging
(ii) Image Coregistration and Multi-Modality of regions of interest
(iii) Extract Radiomic features such as (image intensity, texture, shape etc)
(iv) Obtain statistical analysis and data mining.

Materials and Methods
Method
MRI database
The MRI data was obtained from
a. The Cancer Genome Atlas Glioblastoma Multifome (TCGA-GBM).
b. The Cancer Imaging Archive (TCIA)
The image data of 441 subjects with gliomas were obtained from The Cancer Imaging Archive (Clark *et al.,* 2013). The Cancer Imaging Archive. Overall, 209 subjects, including 124 cases of Glioblastoma and including 85 cases of lower grade glioma from the TCGA-GBM and TCGA-LGG collection (Scarpace*et al.,* 2016) and 200 LGG cases from the TCGA-LGG collection (Pedano*et al.,* 2016).

The clinical dataset used was downloaded from The Cancer Atlas Glioblastoma Multifome (TCGA-GBM) site and also MATLAB code was downloaded from MR Radiomics platform, developed by Chia-Fenglu. The dataset downloaded from TCGA-GBM site (The cancer genome Atlas Glioblastoma

Multifome), MATLAB application was launched and path set to perform image coregistration, resolution adjustment, multi-modalities of region of interest and extraction of radiomics features were performed, the images are shown Figure 2 and 3. The methodology consists of the phases as shown in the methodology flow chart in figure 1.
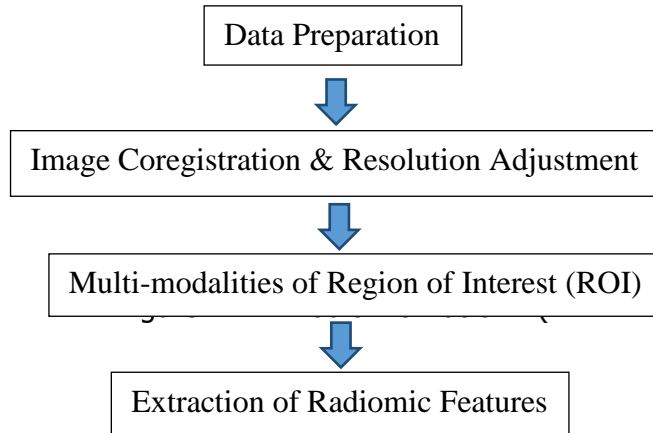
Data Preparation

↓

Image Coregistration & Resolution Adjustment

↓

Multi-modalities of Region of Interest (ROI)

↓

Extraction of Radiomic Features

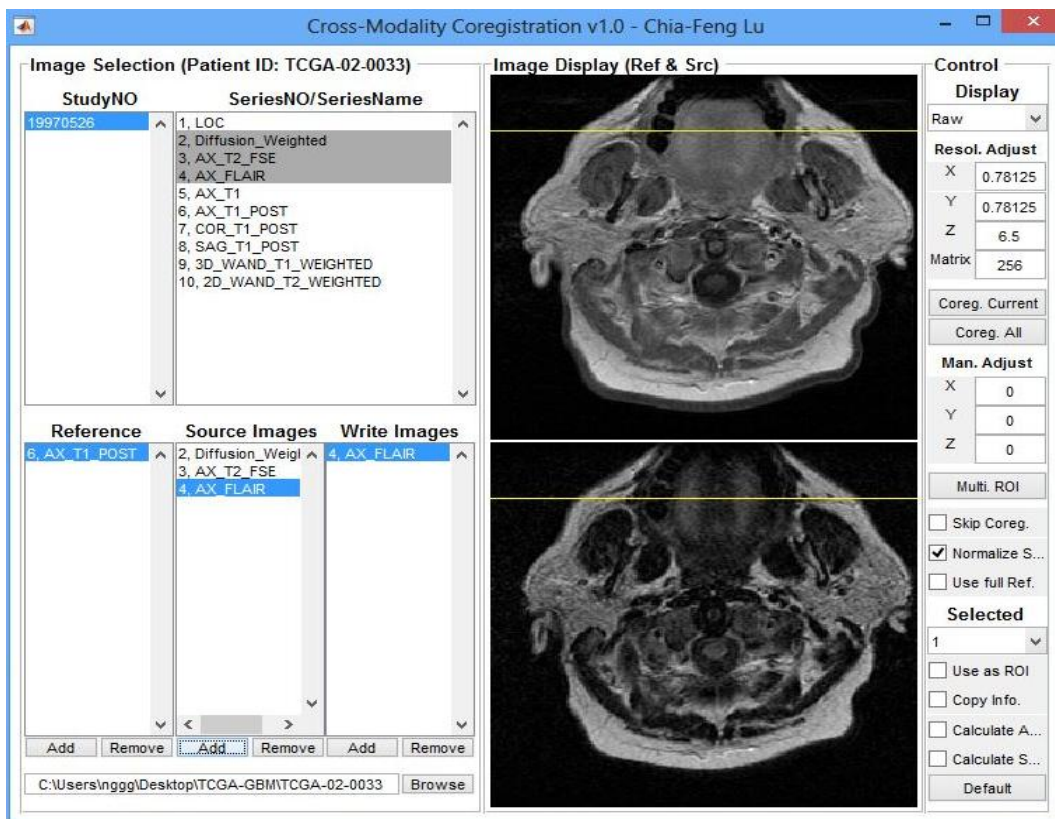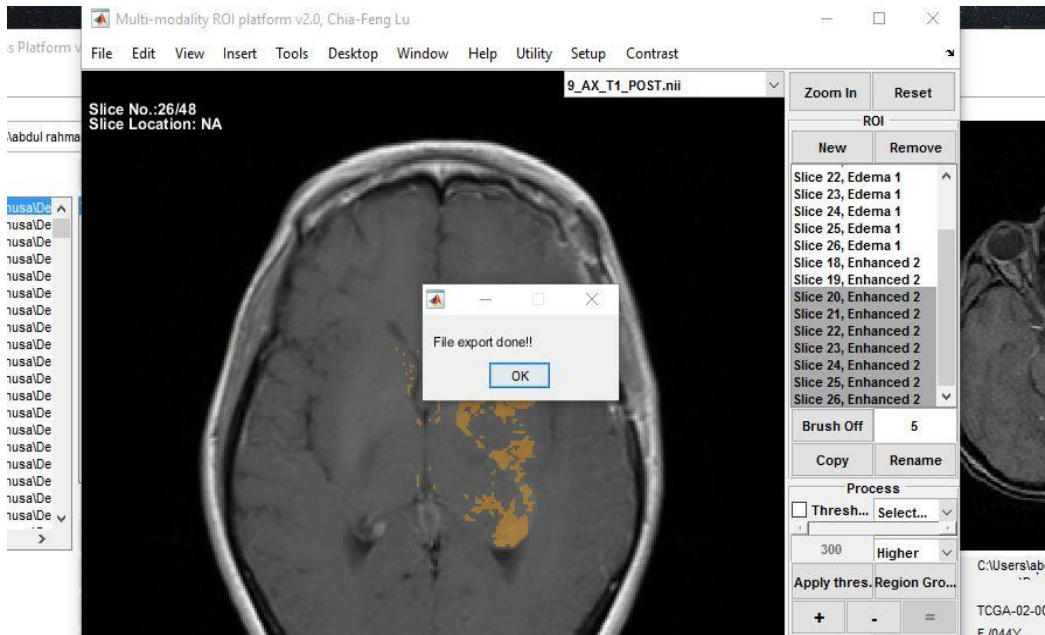**Figure 1: MR Radiomic Platform (MRP-V4S)**

Figure 2: MRP platform showing cross-modalities for choosing reference and source images

Figure 3: Multi-modality ROI GUI after image files export.

Results and Discussion

Radiomics analyses were applied to the image sequences using different configurations of low-pass and high-pass filters. The data extracted are summarized in Tables 1-5.

Table 1: Coordinate, Intensity and ROI of TCGA-02-0033 AX-T1-POST.nii

Patient ID	Series Description		
TCGA-02-0033	6_AX_T1_POST.nii		
Pixel Number	Area (mm^2)	Volume (mm^3)	
11060	6221.25	18663.75	
Mean	Std	Min	Max
0.314463	0.057029	0.25	0.671
Coordinate (r,c,s)	Intensity	ROI	
96, 103, 29	0.252667	Slice 29, Eh 2	
97, 103, 29	0.255333	Slice 29, Eh 2	
99, 103, 29	0.254333	Slice 29, Eh 2	
97, 104, 29	0.255	Slice 29, Eh 2	
99, 104, 29	0.252333	Slice 29, Eh 2	
102, 104, 29	0.256333	Slice 29, Eh 2	
88, 105, 29	0.265	Slice 29, Eh 2	
89, 105, 29	0.265333	Slice 29, Eh 2	
90, 105, 29	0.252	Slice 29, Eh 2	

Coordinate	Intensity	ROI
97, 105, 29	0.252333	Slice 29, Eh 2
102, 105, 29	0.255667	Slice 29, Eh 2
103, 105, 29	0.254	Slice 29, Eh 2
92, 106, 29	0.251333	Slice 29, Eh 2
93, 106, 29	0.250333	Slice 29, Eh 2
97, 106, 29	0.252	Slice 29, Eh 2
99, 106, 29	0.251667	Slice 29, Eh 2
103, 106, 29	0.254333	Slice 29, Eh 2
97, 107, 29	0.252333	Slice 29, Eh 2
98, 107, 29	0.255	Slice 29, Eh 2
99, 107, 29	0.255667	Slice 29, Eh 2
122, 107, 29	0.260333	Slice 29, Eh 2
97, 108, 29	0.252333	Slice 29, Eh 2
98, 108, 29	0.255333	Slice 29, Eh 2
99, 108, 29	0.254333	Slice 29, Eh 2
122, 108, 29	0.265	Slice 29, Eh 2
123, 108, 29	0.289	Slice 29, Eh 2
99, 109, 29	0.251667	Slice 29, Eh 2
105, 109, 29	0.260333	Slice 29, Eh 2
106, 109, 29	0.255667	Slice 29, Eh 2
123, 109, 29	0.289333	Slice 29, Eh 2
124, 109, 29	0.254667	Slice 29, Eh 2
106, 110, 29	0.259333	Slice 29, Eh 2
106, 111, 29	0.252333	Slice 29, Eh 2

Table 2: Coordinate, Intensity and ROI of TCGA-02-0033 reg_2_Diffusion_Weighted.nii

Patient ID	Series Description		
TCGA-02-0033	reg_2_Diffusion_Weighted.nii		
Pixel Number	Area (mm^2)	Volume (mm^3)	
11060	6221.25	18663.75	
Mean	Std	Min	Max
0.17914	0.033733	0.035376	0.351429
Coordinate (r,c,s)	Intensity	ROI	
96, 103, 29	0.126262	Slice 29, Eh 2	
97, 103, 29	0.131235	Slice 29, Eh 2	
99, 103, 29	0.148898	Slice 29, Eh 2	
97, 104, 29	0.125129	Slice 29, Eh 2	
99, 104, 29	0.14315	Slice 29, Eh 2	
102, 104, 29	0.173184	Slice 29, Eh 2	
88, 105, 29	0.161425	Slice 29, Eh 2	
89, 105, 29	0.166201	Slice 29, Eh 2	
90, 105, 29	0.173902	Slice 29, Eh 2	
97, 105, 29	0.122508	Slice 29, Eh 2	
102, 105, 29	0.167263	Slice 29, Eh 2	
103, 105, 29	0.166635	Slice 29, Eh 2	

92, 106, 29	0.163097	Slice 29, Eh 2
93, 106, 29	0.153342	Slice 29, Eh 2
97, 106, 29	0.124963	Slice 29, Eh 2
99, 106, 29	0.13835	Slice 29, Eh 2
103, 106, 29	0.157858	Slice 29, Eh 2
97, 107, 29	0.130245	Slice 29, Eh 2
98, 107, 29	0.133417	Slice 29, Eh 2
99, 107, 29	0.136729	Slice 29, Eh 2
122, 107, 29	0.173203	Slice 29, Eh 2
97, 108, 29	0.133751	Slice 29, Eh 2
98, 108, 29	0.132744	Slice 29, Eh 2
99, 108, 29	0.132703	Slice 29, Eh 2
122, 108, 29	0.173294	Slice 29, Eh 2
123, 108, 29	0.185854	Slice 29, Eh 2
99, 109, 29	0.128231	Slice 29, Eh 2
105, 109, 29	0.154489	Slice 29, Eh 2
106, 109, 29	0.15237	Slice 29, Eh 2
123, 109, 29	0.174409	Slice 29, Eh 2

Table 3: Coordinate, Intensity and ROI of TCGA-02-033 reg_3_AX_T2_FSE.nii

Patient ID	Series Description		
TCGA-02-0033	reg_3_AX_T2_FSE.nii		
Pixel Number	Area (mm^2)	Volume (mm^3)	
11060	6221.25	18663.75	
Mean	Std	Min	Max
0.455643	0.094709	0.07477	0.794118
Coordinate (r,c,s)	Intensity	ROI	
96, 103, 29	0.254075	Slice 29, Eh 2	
97, 103, 29	0.238838	Slice 29, Eh 2	
99, 103, 29	0.227498	Slice 29, Eh 2	
97, 104, 29	0.245571	Slice 29, Eh 2	
99, 104, 29	0.222537	Slice 29, Eh 2	
102, 104, 29	0.250532	Slice 29, Eh 2	
88, 105, 29	0.426293	Slice 29, Eh 2	
89, 105, 29	0.386605	Slice 29, Eh 2	
90, 105, 29	0.357902	Slice 29, Eh 2	
97, 105, 29	0.250532	Slice 29, Eh 2	
102, 105, 29	0.255493	Slice 29, Eh 2	
103, 105, 29	0.283841	Slice 29, Eh 2	
92, 106, 29	0.322112	Slice 29, Eh 2	
93, 106, 29	0.328136	Slice 29, Eh 2	
97, 106, 29	0.254784	Slice 29, Eh 2	
99, 106, 29	0.220057	Slice 29, Eh 2	
103, 106, 29	0.274628	Slice 29, Eh 2	
97, 107, 29	0.260099	Slice 29, Eh 2	

98, 107, 29	0.236003	Slice 29, Eh 2
99, 107, 29	0.219348	Slice 29, Eh 2
122, 107, 29	0.325656	Slice 29, Eh 2
97, 108, 29	0.249823	Slice 29, Eh 2
98, 108, 29	0.230333	Slice 29, Eh 2
99, 108, 29	0.21297	Slice 29, Eh 2
122, 108, 29	0.337349	Slice 29, Eh 2
123, 108, 29	0.38129	Slice 29, Eh 2
99, 109, 29	0.210489	Slice 29, Eh 2
105, 109, 29	0.330262	Slice 29, Eh 2
106, 109, 29	0.351524	Slice 29, Eh 2
123, 109, 29	0.399008	Slice 29, Eh 2

Table 4: Coordinate, Intensity and ROI of TCGA-02-033 reg_3_AX_T2_FLAIR.nii

Patient ID	Series Description	
TCGA-02-0033	reg_3_AX_T1_FLAIR.nii	

Pixel Number	Area (mm^2)	Volume (mm^3)	
11060	6221.25	18663.75	

Mean	Std	Min	Max
0.505553	0.098189	0.104697	0.851745

Coordinate (r,c,s)	Intensity	ROI
96, 103, 29	0.29756	Slice 29, Eh 2
97, 103, 29	0.278667	Slice 29, Eh 2
99, 103, 29	0.267909	Slice 29, Eh 2
97, 104, 29	0.284965	Slice 29, Eh 2
99, 104, 29	0.262398	Slice 29, Eh 2
102, 104, 29	0.295329	Slice 29, Eh 2
88, 105, 29	0.465495	Slice 29, Eh 2
89, 105, 29	0.434138	Slice 29, Eh 2
90, 105, 29	0.406193	Slice 29, Eh 2
97, 105, 29	0.290213	Slice 29, Eh 2
102, 105, 29	0.294542	Slice 29, Eh 2
103, 105, 29	0.32708	Slice 29, Eh 2
92, 106, 29	0.370638	Slice 29, Eh 2
93, 106, 29	0.375623	Slice 29, Eh 2
97, 106, 29	0.295592	Slice 29, Eh 2
99, 106, 29	0.256494	Slice 29, Eh 2
103, 106, 29	0.318158	Slice 29, Eh 2

Table 5: The clinical characteristics of the training datasets

Subtypes	LGG IDH mut-codel	LGG IDH mut-noncodel	LGG IDH wt	GBM IDH mut	GBM IDH wt
Subject number	30 (29.2% of LGG)	47 (56.6% of LGG)	31 (21.2% of LGG)	9 (7.3% of GBM)	90 (92.5% of GBM)
2016 WHO entity	Oligodendroglioma/ anaplastic	Diffuse/anaplastic astrocytoma, IDH	Diffuse astrocytoma, IDH wt;	GBM, IDH	GBM, IDH

	oligodendroglioma, IDH mut-code	mut	oligodendroglioma, NOS	mut	wt
Histology					
Astrocytoma	0 (0%)	22 (39.3%)	10 (47.6%)	0 (0%)	0 (0%)
Oligoastrocytoma	4 (12.9%)	19 (33.9%)	3 (14.3%)	0 (0%)	0 (0%)
Oligodendroglioma	23 (89.1%)	15 (26.8%)	8 (38.1%)	0 (0%)	0 (0%)
Glioblastoma	0 (0%)	0 (0%)	0 (0%)	8 (100%)	98 (100%)
ATRX status					
Wild type	47 (96.8%)	18 (32.1%)	32 (100.0%)	3 (37.5%)	53 (54.1%)
Mutation	1 (3.2%)	38 (67.9%)	0 (0%)	3 (37.5%)	1 (1.0%)
Unknown	0 (0%)	0 (0%)	0 (0%)	2 (25%)	44 (44.9%)
Age at diagnosis (years) Mean (SD)	51.7 (13.2)	40.2 (12.4)	52.5 (12.3)	39.0 (15.9)	60.8 (12.1)
Survival (months) Mean (95% CI)	57.8 (40.6–74.9)	90.0 (62.6–115.3)	48.0 (12.1–83.9)	32.7 (19.2-46.2)	15.0 (12.6–17.5)
Karnofsky performance scale					
100	3 (9.7%)	9 (16.0%)	1 (4.8%)	3 (37.5%)	12 (12.3%)
90	6 (19.4%)	17 (30.4%)	8 (38.1%)	0	1 (1.0%)
70–80	3 (9.7%)	7 (12.5%)	4 (19.0%)	4 (50.0%)	50 (51.0%)
<70	2 (6.5%)	2 (3.6%)	0 (0%)	0	17 (17.3%)
Unknown	17 (54.7%)	21 (37.5%)	8 (38.1%))	1 (12.5%)	18 (18.4%)

Table 5 shows the clinical characteristics and the relevant subtypes of the 209 included glioma subjects in the training dataset. For LGG, the most prevalent subtype is LGG-IDH mutant-non codel (56.6%), followed by LGG-IDH mutant-codel (29.2%) and LGGIDH wild-type (21.2%). Most of the subjects with GBM had the GBM IDH wide-type subtype (92.5%), which shows the poorest overall survival (average of 13.0 months) among all glioma subtypes. Only a small cohort of GBM subjects (7.3%) had the GBM-IDH wild-type subtype, which has a mean survival of 30 months. Most LGG-IDH mutant codel gliomas were Oligodendroglioma (89.1%) with wild-type ATRX (47/48 cases, 96.8%).

Table 6: Model performance for the Binary classifier estimated on the training dataset

| Classification (Subject number)	Required Images Contrast	Area Under Curve (AUC)	Accuracy	Specificity	Sensitivity
GBM vs LGG (209 Subject)	Ensemble Bagged Tree/T_1+C, T_2 FLAIR	0.98	68.6%	92.0%	86.0% (true rate for LGG)
DH wt vs. mut in GBMs (64 subjects).	Cubic SVM/ T_1 + C, T_1 POST	0.99	80.1%	95.5% (true rate for wt)	100.0% (true rate for mut)
IDH wt vs. mut in LGGs (45 subjects)	T_1+C, Diffusion Weighted	0.81	78.5%	85.7% (true rate for wt)	93.0% (true rate for mut)
1p/19q noncodel vs. codel in IDH mut LGGs (81 subjects) T2W	Quadratic SVM/T_1+C, T_2 FSE,	0.95	87.7%	88.5% (true rate for noncodel)	86.2% (true rate for codel) 0.768

The performance of the Eleven-level binary classification model of the selected radiomics features, classification learner was applied, reference was plotted against intensities, with eleven predictors (Intensities), six classes response (System) and 25% Hideout Validation of the training dataset.

Classification learner was applied to multi modal of the low- high spatial frequency of wavelength decomposition to the selected radiomics features in the differentiation of LGG/GBM, IDH, and the 1p/19q status of gliomas are shown in table 6. Eleven machine-learning models were chosen, and the highest accuracy of the models was Ensemble (Bagged Tree) selected for the classification of histology (LGG vs. GBM,), the Cubic SVM has the highest accuracy for the classification of IDH status in LGG, the cubic SVM for the classification of IDH status in GBM, and the Quadratic SVM for the classification of 1p/19q status in IDH mutation LGG. The predictive model scores estimated by the selected machine-learning models. The disparities between the predictive scores of the groups show the ability of the machine learning models to transfer radiomic features into a differentiable value for effective classification. The machine-learning models can achieve satisfactory classifications with AUCs between 0.81 and 0.99 estimated using the training dataset.
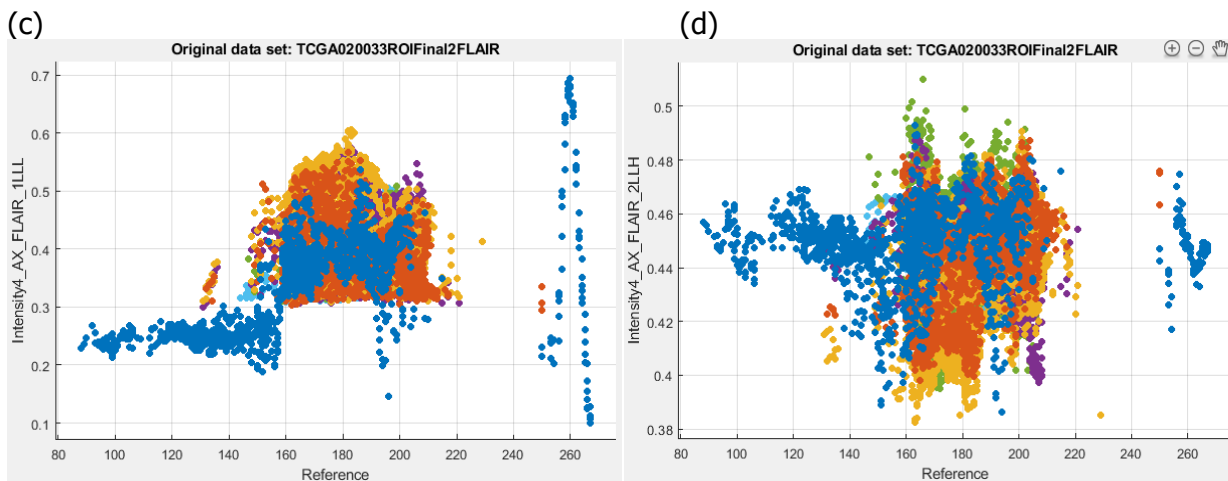
(a)   (b)
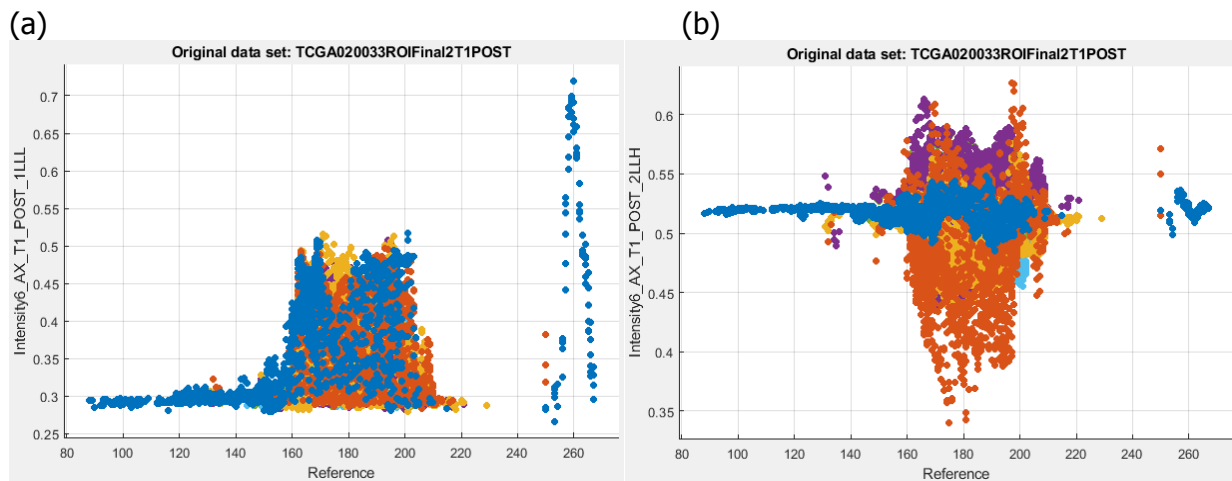
Figure 4: Plot of image intensity (AX_T1_POST image) for (a) low-pass filters applied in three directions (b) low-pass filter applied in one direction and high-pass filters applied in two directions.

(c)   (d)
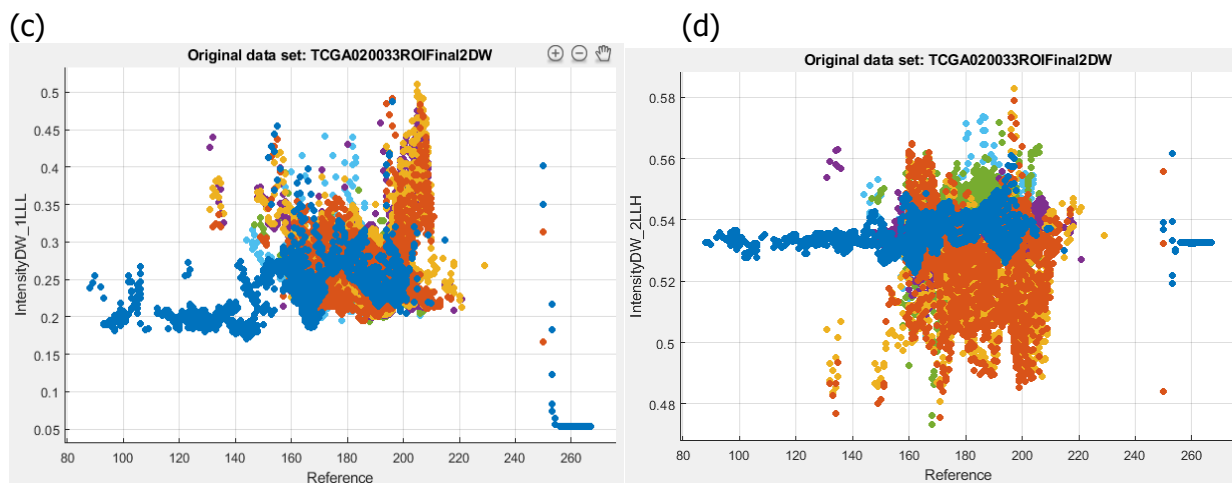
Figure 5: Plot of image intensity (diffusion-weighted (DW) image) for (a) low-pass filters applied in three directions (b) high-pass filter applied in one direction and low-pass filters applied in two directions.

(a)

(b)
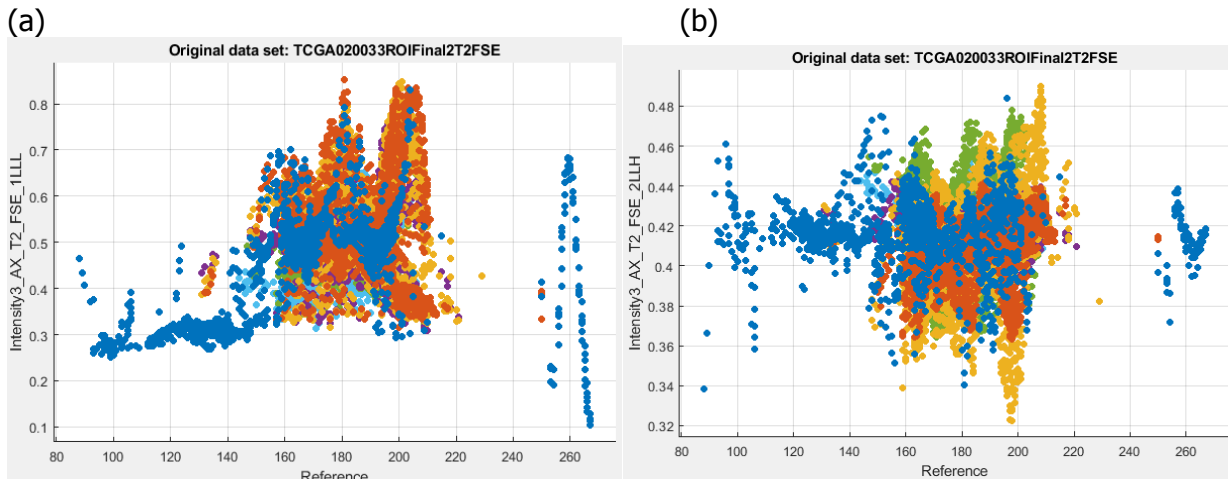
Figure 6: Plot of image intensity (AX_T2_FSE image) for (a) low-pass filters applied in three directions (b) high-pass filter applied in one direction and low-pass filters applied in two directions.

(c)

(d)

Figure 7: Plot of image intensity (AX_FLAIR image) for (a) low-pass filters applied in three directions (b) high-pass filter applied in one direction and low-pass filters applied in two directions.

The visualizations for the data presented in Tables 1-4 are presented in Figures 4-7. These figures show the distributions of image intensity for different configurations of low-pass and high-pass filters. These figures show the variations of image intensity across the reference coordinates based on the number and type of pass filters applied. These visualizations could prove to be very useful in identifying reference points for different tissues especially those with diseases. It is important to note that features that are not conspicuous on one MRI sequence will definitely show clearly on the other sequences especially after application of wavelet decompositions.

Conclusion
Brain tumor is a rapidly growing disease that affects the normal functions of the brain. The results in Table 5 and 6 clearly presents a workable MRP Radiomic approach to predicts, detects and diagnose brain tumor easily. This platform is essential in characterizing, visualizing and gives adequate information on brain tumors. It also helps radiologist to analysis clinical images; and shows ways for treating patient according their tumor grade level (I-IV). MRP 4 software extracted more than 11062

features that comprises of the first texture histogram, shape and size, gray level co-occurrence matrix, gray level run length matrix etc. The mean, minimum mean, maximum mean, standard deviation, area and volume of the brain tumor were also calculated, which gives detailed insight into brain tumors. The results from this study shows how MR radiomics can actually differentiate GBMs from LGGswhich makes the work of Doctors and Radiologist simpler and easier, and also reducing the mortality rate of cancer patient by predicting anddetecting of brain tumors early enough for immediate therapy. Meanwhile, this software can be extended to other diseases such as breast cancer, lung and abdominal pain, for analysis and demonstrating data mining opportunities provided by MRP.

References

Clark, K., Vendt, B., Smith, K., Freymann, J., Kirby, J., Koppel, P., Moore, S., Phillips, S., Maffitt, D., Pringle, M.,& Prior, F. (2013). The Cancer Imaging Archive (TCIA): maintaining and operating a public information repository. *Journal of Digital Imaging*, *26*(6), 1045-1057.

Ganguly, D., Chakraborty, S., Balitanas, M., & Kim, T. H. (2010). Medical imaging: A review. In *International Conference on Security-Enriched Urban Computing and Smart Grid* (pp. 504-516). Springer, Berlin, Heidelberg.

Giger, M. L. (2018). Machine learning in medical imaging. *Journal of the American College of Radiology, 15(3), 512-520.*

Kanade, P.B., &Gumaste.(2015).Brain tumor detection using MRI images. *Brain 3, (2), 146-150.*

Lambin, P., Rios-Velazquez, E., Leijenaar, R., Carvalho, S., Van Stiphout, R. G., Granton, P., Zegers, C.M., Gillies, R., Boellard, R., Dekker, A.,&Aerts, H. J. (2012). Radiomics: extracting more information from medical images using advanced feature analysis. *European Journal of Cancer*, *48(4), 441-446.*

Lu, C. F., Hsu, F. T., Hsieh, K. L. C., Kao, Y. C. J., Cheng, S. J., Hsu, J. B. K., Tsai, P.H., Chen, R.J., Huang, C.C., Yen, Y.,& Chen, C. Y. (2018). Machine learning–based radiomics for molecular subtyping of gliomas. *Clinical Cancer Research, 24(18), 4429-4436.*

Merrell, R. T. (2012). Brain Tumors. *Disease-a-Month*, *58(12), 678-689.*

Pedano, N., Flanders, A. E., Scarpace, L., Mikkelsen, T., Eschbacher, J. M., Hermes, B., &Ostrom, Q. (2016). Radiology data from the cancer genome atlas low grade glioma [TCGA-LGG] collection. *The cancer imaging archive*, *2.*

Scarpace, L., Mikkelsen, L., Cha, T., Rao, S., Tekchandani, S., Gutman, S., & Pierce, D. (2016). Radiology data from the cancer genome atlas glioblastoma multiforme [TCGA-GBM] collection. *The Cancer Imaging Archive*, *11*(4), 1.

The Cancer Imaging Archive (TCIA). Accessed online on 9th June 2019 from http://www. cancerimagingarchive.net/

Yip, S. S., Liu, Y., Parmar, C., Li, Q., Liu, S., Qu, F., Ye, Z., Gillies, R. J., & Aerts, H. J. (2017). Associations between radiologist-defined semantic and automatically computed radiomic features in non-small cell lung cancer. *Scientific Reports*, *7*(1), 1-11.